Dalton Transactions

ROYAL SOCIETY OF CHEMISTRY

PAPER

View Article Online
View Journal

Cite this: DOI: 10.1039/d6dt00442c

Novel non-symmetric POCOP–Ni(II) pincer complexes derived from 2,4-dihydroxybenzaldehyde

Jordi R.-Galindo, [a] Jhon Sebastian Oviedo-Ortiz,[a] Antonino Arenaza-Corona, [a] Adrián Ruíz-Martínez, [a] Juan S. Serrano-García, [a] Simón Hernández-Ortega,[a] Marcos Flores-Alamo, [b] T. Keith Hollis [c] and David Morales-Morales *[a]

Received 20th February 2026,
Accepted 17th March 2026

DOI: 10.1039/d6dt00442c

rsc.li/dalton

Pincer ligands have long captivated chemists for their ability to merge rigidity, modularity, and fine-tuned electronic control into a single molecular scaffold. Within this class, POCOP-type ligands stand out for their capacity to stabilize reactive metal centers while enabling diverse catalytic and functional applications. Yet, the deliberate rupture of symmetry in these systems—particularly in non-symmetric POCOP frameworks—remains an underexplored route to unlocking new reactivity patterns. Herein, we report the synthesis of a family of non-symmetric Ni(II)–POCOP pincer complexes (**2a–2c**) and demonstrate that their formation is decisively governed by the presence or absence of base during the metalation step. Under basic conditions, selective formation of the aldehyde-type pincer complexes is achieved, whereas base-free conditions lead to acid-promoted ligand activation and the formation of imine-type addition complexes (**3a–4c**), which may partially hydrolyze during purification to yield aldehyde-type addition complexes (**5a–5c**). The structures and coordination modes of the isolated species were established by comprehensive spectroscopic methods and single-crystal X-ray diffraction. Subsequent optimization of the reaction conditions enabled the selective synthesis of the target non-symmetric Ni(II)–POCOP complexes in improved yield and purity, providing insight into the role of medium acidity in directing the stability and reactivity of phosphinite-based pincer systems.

1 Introduction

Pincer ligands have become a central motif in organometallic chemistry due to their strong metal–ligand interactions,[1,2] structural rigidity,[3] and tunable electronic and steric properties.[4] Since the seminal work of Shaw and Moulton in the late 1970s,[5,6] pincer-type scaffolds have attracted considerable attention. These ligands are typically defined as tridentate frameworks that coordinate a metal center in a meridional fashion.[1] Such architectures enable the formation of robust organometallic species with remarkable thermal and chemical stability.[4,7] These features have made pincer complexes highly versatile platforms in homogeneous catalysis,[8–11] C–H bond activation,[12,13] and metallodrug development.[14,15]

Traditionally, most pincer ligands are symmetric, featuring identical donor arms that confer well-defined coordination environments and predictable reactivity patterns.[4] However, the increasing need to fine-tune metal-centered properties has spurred growing interest in non-symmetric pincer systems.[16,17] In these ligands, electronic and steric asymmetry introduced by distinct donor groups or substituents enables modulation of metal–ligand cooperation, redox behavior, and catalytic selectivity.[16,18,19] Consequently, non-symmetric pincers provide access to a broader chemical space and facilitate the rational design of complexes with tailored reactivity profiles.

Symmetry rupture in pincer ligands can be achieved basically through three distinct strategies.[3,4,16] The first involves introducing different lateral donor groups, leading to motifs such as SCN,[20] PCN,[21] PCP′,[22] or NNP.[23] The second approach involves modification of the linker atoms, which can give rise to PXCYP architectures (*e.g.*, POCNP,[24] PSCOP,[25] PCCOP[26]) or to ligands featuring most commonly fused metallacycles with five- and six-membered rings.[27,28] These examples illustrate commonly reported strategies reported in the literature, but are by no means exhaustive; for a more comprehensive discussion, specialized reviews should be consulted.[16,29] Although these two approaches are noteworthy, the present work focuses primarily on the third symmetry rupture strategy, which can be achieved through modification of the pincer backbone.

Among the different families of pincer ligands, those containing phosphorus donors and oxygen linkers—such as POCOP-type frameworks—have attracted considerable atten-

[a]*Instituto de Química, Universidad Nacional Autónoma de México, Cd. Universitaria, Circuito Exterior, Coyoacán, CDMX, C.P. 04510, Mexico. E-mail: damor@unam.mx*
[b]*Facultad de Química, Universidad Nacional Autónoma de México, CDMX 04510, Mexico*
[c]*Department of Chemistry, Mississippi State University, MS, 39762, USA*

tion for their ability to stabilize both low- and high-valent metal centers.[30,31] Incorporating non-symmetry into these scaffolds offers additional control over the metal coordination environment and cooperative effects during catalysis.[27,32,33] Despite this promise, systematic studies on the synthesis, structural characterization, and reactivity of non-symmetric pincer complexes remain relatively scarce, in part due to the synthetic challenges associated with their preparation and purification.

For instance, several reports describe non-symmetric POCOP-type pincer complexes in which the lack of symmetry originates from the introduction of different substituents at the *meta* position of the pincer ligand.[27,34–39] One of the earliest examples in this series includes complexes **Ia–IIIb** (Chart 1), whose catalytic activity was evaluated in C–C cross-coupling reactions. Notably, complex **IIb** exhibited excellent performance in the Mizoroki–Heck reaction, achieving conversions of up to 99%.[34] Moreover, the catalytic activity of complexes **IVa–Vb**[36] was evaluated in the synthesis of diaryl ketones. Among these, complex **Va** exhibited the highest activity, reaching 98.5% conversion with only 1 mol% catalyst loading. Finally, one of the first examples of C–P bond formation *via* hydrophosphorylation was reported for complexes **VIa** and **VIb**.[37]

Beyond their catalytic applications, the biological properties of non-symmetric pincer complexes have also been reported. For example, complex **VIIc**[38] displayed notable antibacterial activity with a minimum inhibitory concentration (MIC) of 8 μg mL^{-1} against *S. aureus* ATCC 25923. Molecular docking studies revealed low binding energies with the PBP2A protein, suggesting that metal coordination enhances the complex's affinity toward DNA, gultathione (GSH), and proteins compared to the free ligands.

In this context, we report the synthesis and characterization of a new series of non-symmetric POCOP-type pincer complexes that are designed to elucidate the influence of electronic asymmetry on their coordination behavior and metal-centered reactivity. The study comprised the preparation of three non-functionalized and nine functionalized complexes, whose structures were characterized by spectroscopic techniques; notably, eight of them were confirmed by single-crystal X-ray diffraction. To obtain the target non-functionalized Ni(II)–POCOP pincer complexes **2a–2c**, a modified and optimized synthetic methodology was developed based on previously reported procedures.[36–38,40] Interestingly, during these reactions, additional functionalized unexpected products were isolated in which a C–P bond was formed, corresponding to imine-type (**3a–4c**) and aldehyde-type (**5a–5c**) addition complexes.

2 Results and discussion

2.1 Synthesis and characterization

Initially, we attempted to synthesize complexes **2a–2c** starting from 2,4-dihydroxybenzaldehyde (**2,4-DHBA**), as depicted in Scheme 1; however, the desired complexes were not obtained (see Fig. S1 and S2). This outcome is attributed to the electron-withdrawing nature of the *meta*-substituted aldehyde, which likely deactivates the aromatic ring toward C–H activation and hinders Ni–C bond formation. Inspired by previously reported methodologies,[36–38] we therefore prepared a series of Schiff base derivatives (**1a** and **1b**) bearing *n*-propyl or *tert*-butyl substituents. These modifications were expected to attenuate the electron-withdrawing character of the proligand backbone and—particularly in the case of **1b**—to provide steric protection, thereby facilitating Ni–C bond formation through increased electron density at the *ipso* carbon.

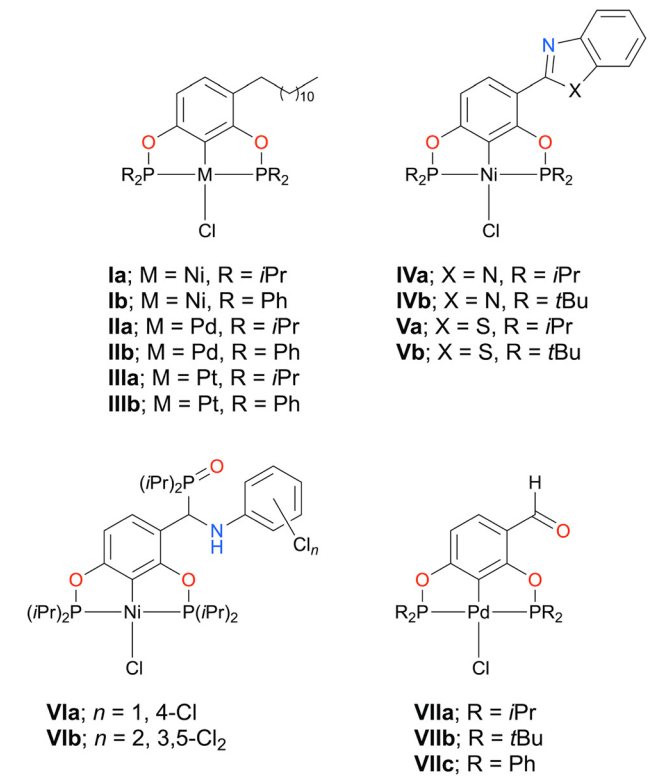

Chart 1 Previously reported non-symmetric group 10-POCOP pincer complexes.

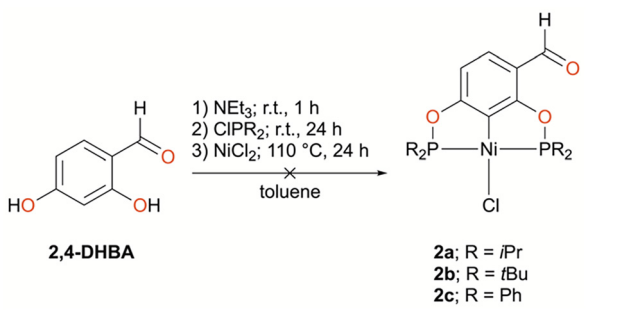

Scheme 1 Attempted synthesis of complexes **2a–2c** from precursor **2,4-DHBA**.

Imine precursors **1a** and **1b**, previously reported in the literature,[41–43] were synthesized following a modified procedure developed by our group[38] (Scheme 2) and used as starting materials. Briefly, acid-catalyzed condensation of 2,4-dihydroxybenzaldehyde (**2,4-DHBA**) with the corresponding amine afforded the target imines. Using this methodology, compounds **1a** and **1b** were obtained in a straightforward manner, with shorter reaction times and higher yields than those previously reported.

Complexes **2a–2c** were synthesized from precursors **1a** or **1b** following modified literature procedures.[38,40] As shown in Scheme 3, the corresponding POCOP-type proligand was obtained by reaction of the imine precursor with the appropriate chlorophosphine in the presence of base. Subsequent metallation with $NiCl_2$ under reflux afforded complexes **2a–2c**. Full experimental details are provided in section 6.2.

Under these reaction conditions, complexes **3a–5c** were unexpectedly obtained. These species correspond to the imine-type addition complexes (**3a–3c** or **4a–4c**, depending on the imine precursor) and, exclusively from **1a**, aldehyde-type addition complexes (**5a–5c**). The yields of complexes **2a–2c** obtained from imine **1a** were 15, 30, and 3%, respectively, while those obtained from imine **1b** were 22, 37, and 11%, respectively. For complex **4a**, a yield of 53% was obtained, whereas complexes **3a–3c**, **4b**, **4c** and **5a–5c** were isolated only in trace amounts.

Scheme 2 Synthesis of compounds **1a** and **1b**.

Due to the low isolated yields of the addition products (**3a–3c**, **4b**, **4c** and **5a–5c**), sufficient material for spectroscopic characterization was obtained by combining the corresponding chromatographic fractions from multiple independent reactions prior to analysis. The comparatively higher yield observed for **4a** is attributed to a combination of steric effects associated with both the phosphorus substituents and the imine moiety. In particular, the lower steric demand of the iPr substituent at phosphorus, present in both the phosphinite and the phosphine oxide functionalities, facilitates formation of the addition complex. In contrast, increased steric congestion associated with bulkier substituents reduces the stability of reactive intermediates and promotes decomposition under the reaction conditions.

Steric effects associated with the phosphorus substituents appear to influence the formation of the addition complexes (**3a–4c**). Product formation is favored when steric congestion at phosphorus remains sufficiently low to allow access to the metal coordination site.[44] In this context, the iPr-substituted phosphinite system provides a steric environment that can facilitate effective metal–ligand interaction and promote the reaction pathway leading to addition complex formation.[45,46] In contrast, increased steric bulk at phosphorus may restrict access to the reactive metal center, disfavoring formation of several of the corresponding addition products (**3a–3c**, **4b** and **4c**), which are obtained only in trace amounts.[47]

Electronic effects associated with the phosphorus substituent further modulate this steric influence. The iPr group combines moderate σ-donation with relatively low steric encumbrance, providing a balance that may stabilize key intermediates involved in the addition process. In contrast, although the *t*Bu substituent exhibits stronger σ-donor character, it also introduces substantial steric congestion that may hinder stabilization and formation of the corresponding addition intermediates. The Ph substituent, while less sterically demanding than *t*Bu, is a weaker σ-donor due to π-delocalization, which

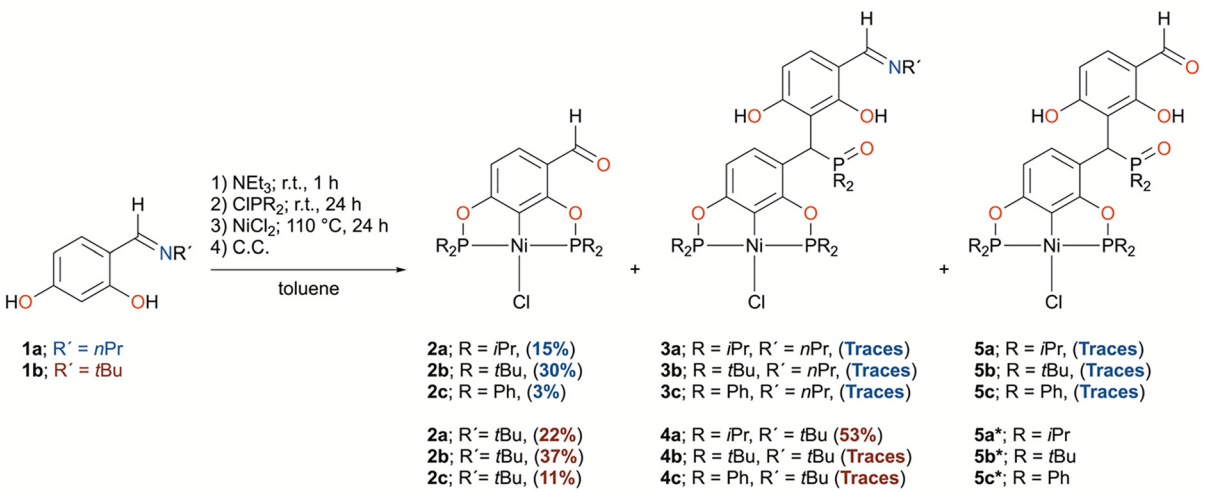

Scheme 3 Synthesis of pincer complexes: **2a–2c** and **3a–5c**. For **2a–5c**, yields obtained from **1a** (R′ = *n*Pr) are shown in blue, and those from **1b** (R′ = *t*Bu) in red, highlighting the influence of the substituent on reaction efficiency. *Not observed.

reduces electron density at phosphorus and weakens metal–ligand bonding.[48,49] Consequently, the donor strength of the phosphinite moiety is diminished, which may disfavor both the initial metal–ligand association and subsequent transformations leading to the formation of imine-type addition complexes.[45–47,50] These observations suggest that both steric accessibility and the donor properties of the phosphorus substituents contribute to the observed reactivity trends.

Within the iPr-substituted series, the preferential formation of **4a** over **3a** highlights the influence of the imine substituent on stabilization of the addition complex. Replacement of the *n*Pr group in **3a** by the more electron-donating and sterically demanding *t*Bu group in **4a** enhances stabilization of the reactive intermediate through a combination of electronic and steric effects.[44] Electronically, the *t*Bu substituent may increase electron density at the imine moiety through inductive donation, which can strengthen metal–ligand interactions in the corresponding addition complex.[51,52] Sterically, the greater bulk of the *t*Bu group may provide kinetic protection against decomposition pathways by partially shielding the reactive site, thereby favoring formation of the addition product. In contrast, the *n*Pr-substituted imine in **3a** provides less electronic stabilization and steric protection, resulting in rapid decomposition and only trace-level formation under identical conditions.

Overall, the combined steric and electronic influences of the phosphorus substituent govern the efficiency of addition complex formation. This trend is consistent with previous studies demonstrating that bulky phosphine- or phosphinite-type donors reduces metal–ligand substitution rates and increases steric congestion near the reactive center.[53–55] Although detailed mechanistic studies were not undertaken, the observed product distributions are consistent with steric control of intermediate accessibility, with electronic effects providing additional fine-tuning of intermediate stability.

Even though the isolated products were initially presumed to correspond to the imine-type pincer complexes based on the reaction conditions, spectroscopic analysis clearly indicated the presence of an aldehyde functionality. For complexes **2a–2c**, the ^{1}H NMR spectrum (see Fig. S7, S11 and S15) exhibited the expected AB signal pattern for the aromatic scaffold, consistent with *meta*-substitution. In addition, a signal at 10.15, 10.19, and 10.29 ppm, respectively, indicates the presence of the aldehyde proton and inconsistent with an imine moiety. In the ^{13}C{^{1}H} NMR spectrum, the signal corresponding to the carbonyl carbon appears at 188.2, 188.4, and 188.0 ppm, respectively, further confirming aldehyde formation. These observations in addition to the mass spectra (see Fig. S10, S14 and S18) indicate that hydrolysis of the imine occurred during chromatographic purification, leading to isolation of an aldehyde-type pincer complexes.

The ^{31}P{^{1}H} NMR spectra (see Fig. S9, S13 and S17) display a characteristic AB patterns consistent of two mutually coupled doublets, reflecting the loss of symmetry within the pincer scaffold upon metal coordination. Importantly, this coupling originates from efficient metal-mediated Fermi contact interaction through the P–Ni–P framework, which provides an effective pathway for spin-density delocalization between the *trans* phosphorus donors.

Large *trans*-phosphorus coupling constants ($^{2}J_{P-P} \approx 300$–375 Hz; see exact values below) are observed in the ^{31}P{^{1}H} NMR spectra. In contrast, related free phosphinite ligands have been reported to display two uncoupled ^{31}P signals,[37] reflecting the absence of an efficient through-bond coupling pathway between phosphorus nuclei. Formation of the P–Ni–P unit establishes an efficient metal-mediated Fermi-contact pathway in which σ-donation from the phosphorus donors into nickel orbitals with appreciable s-character enables delocalization of spin density through the metal center and back to the opposing phosphorus atom, thereby generating a large metal-mediated scalar coupling between the *trans* phosphorus nuclei.[56] This mechanism accounts for the unusually large *trans* $^{2}J_{P-P}$ values observed in related square-planar Ni pincer complexes.[57,58]

Importantly, observation of this effect does not require the metal nucleus itself to be NMR-active; rapid nuclear relaxation associated with quadrupolar or spin-zero nickel isotopes may suppress observable metal satellites, while the electronic pathway responsible for metal-mediated scalar coupling remains fully operative.[57,59]

For complexes **2a** and **2b**, the signals appear at 191, and 194 ppm, respectively, with coupling constants 326.3, and 300.1 Hz, respectively. Interestingly, for **2c** the phosphorus signals shift significantly to 148 ppm and the coupling constants increases to 374.2 Hz. These changes are attributed to the strong π-conjugation between the phosphorus atom and the phenyl ring. In contrast, isopropyl and *tert*-butyl substituents are purely σ-donors, providing electron density only through inductive and hyperconjugative effects without π-delocalization. The increased coupling constant observed for the phenyl derivative is consistent with enhanced π-delocalization, which shortens and strengthens the P–O bond, increases the s-character of phosphorus, and thereby enhances orbital overlap with the metal center.[60]

The ^{1}H NMR spectrum of imine-type addition complex **4a** (see Fig. S31) displays the characteristic iminic proton signal at 7.95 ppm, together with two distinct AB spin systems in the aromatic region. The first AB system, corresponding to the pincer scaffold, appears at 7.60 and 6.35 ppm with a coupling constant of 8.5 Hz. The second AB system is observed at 6.90 and 6.29 ppm with a coupling constant of 8.7 Hz. A doublet at 5.82 ppm is assigned to the methine proton generated upon addition of the phosphine oxide ($^{2}J_{P-H} = 10.7$), which is characteristic for such two-bond couplings.[60]

In the aliphatic region, two closely related sets of signals are observed for the methine and methyl groups of the isopropyl substituents. The first set of signals is associated to the phosphinite moiety of the pincer system and the second set to the newly formed phosphine oxide generated upon addition at the former aldehyde position of **2a**. Although both phosphorus centers bear identical isopropyl substituents, their different electronic environments give rise to similar yet non-identical

chemical shifts for the corresponding aliphatic signals Notably, the signals corresponding to the phenolic protons are shifted downfield relative to those observed for the imine starting material **1b**, consistent with the coordination and hydrogen-bonding effects induced by the metal complexation.

The $^{31}P\{^{1}H\}$ NMR spectrum of **4a** (see Fig. S33) shows, in addition to the characteristic AB system of the pincer ligand at 184 ppm ($^{2}J_{P-P}$ = 324.8 Hz), a singlet at 66 ppm, which is assigned to the phosphine oxide moiety attached to the carbon atom formerly bearing the aldehyde group in **2a**. The DART mass spectrum (Fig. S34) exhibits a molecular ion at *m*/*z* 772, which also corresponds to the base peak, further supporting the assigned composition of **4a**.

Single-crystal X-ray diffraction studies of **3a**, **5b** and **5c** unambiguously confirmed the proposed connectivity and coordination modes of the imine- and aldehyde-type addition complexes. On this basis, the structures of the remaining analogues (**3b**, **3c**, **4b**, **4c** and **5a**) were assigned by analogy, supported by their consistent synthetic behavior, chromatographic properties, and spectroscopic data (^{1}H-NMR, ^{13}C-NMR, ^{31}P-NMR, IR and/or MS, where available).

For the remaining addition complexes—imine-type (**3b**, **3c**, **4b**, and **4c**) and aldehyde-type (**5a**)—full characterization was not possible in all cases due to their low isolated yields. In particular, the identity of **5a** was supported by DART-MS data and by analogy with the crystallographically characterized complexes **5b** and **5c**, which share the same aldehyde-type addition motif. Consistent NMR chemical shift patterns and coupling behaviors within each series further support these structural assignments.

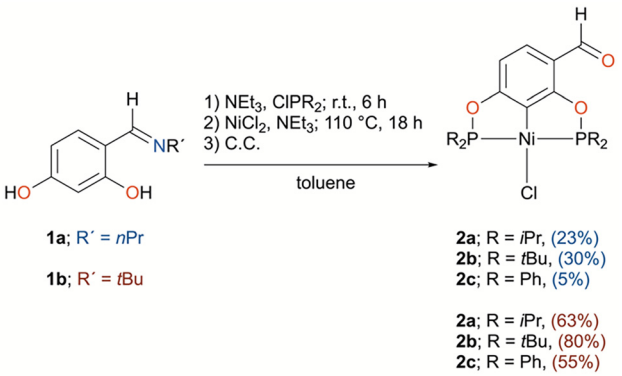

Scheme 4 Synthesis of aldehyde complexes **2a–2c**. Yields obtained from **1a** (R′ = *n*Pr) are shown in blue, and those from **1b** (R′ = *t*Bu) in red, highlighting the effect of the substituent on reaction efficiency.

To optimize the synthesis of aldehyde-type complexes **2a–2c** (Scheme 4), the previous methodology was modified by introducing 1.2 equiv. of triethylamine after adding the solution of the corresponding pincer ligand to a suspension of nickel chloride.[39] The presence of this base facilitated deprotonation and coordination, resulting in a cleaner conversion to the desired products and a significant reduction in the formation of byproducts (**3a–5c**). As result, complexes **2a–2c** were obtained in 63%, 80%, and 55%, respectively, particularly when starting from **1b**, representing a substantial improvement relative to the original conditions (Scheme 3).

2.2 Mechanistic discussion

Although no detailed mechanistic investigations were performed, the observed product distributions allow a plausible reaction pathway to be proposed, consistent with established reactivity patterns of phosphinite ligands, to rationalize the divergent outcomes under basic and non-basic conditions.

Notably, the formation of mixtures containing both aldehyde- and addition-type complexes (**2a–5a**, **2b–5b**, or **2c–5c**, respectively; Scheme 3) or solely aldehyde complexes (**2a–2c**; Scheme 4) appears to depend on the addition of triethylamine (Et_3N) during the metalation step. To rationalize these observations, a plausible reaction mechanism is proposed. As illustrated in Scheme 5, the formation of **6** is accompanied by the liberation of one equivalent of HCl into the reaction medium. When Et_3N is added during the metalation stage, the generated HCl is neutralized, which may suppress further reactivity. Under this conditions, the reaction predominantly affords complex **6**.

In contrast, when Et_3N is omitted during the final metalation step, the HCl generated *in situ* remains unneutralized and may protonate the phosphinite oxygen of the POCOP proligand. Protonation of the P–O moiety increases the polarization of the P–O bond, rendering the phosphorus center more electrophilic and susceptible to nucleophilic attack by chloride. This process may promote cleavage of the P–O bond, leading to partial reversal of ligand formation and regeneration of the imine precursor **1**, together with the liberation of two equiva-

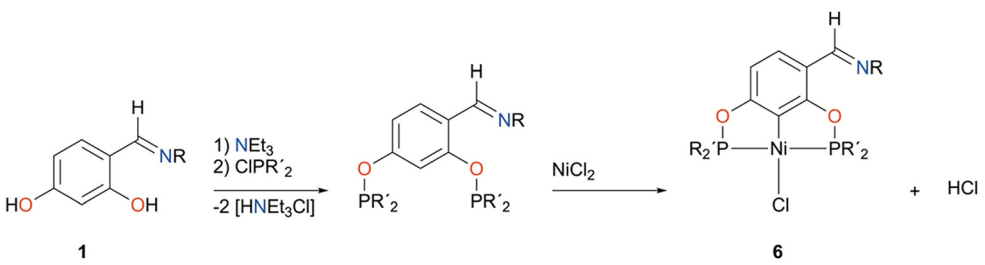

Scheme 5 Reaction step associated with the formation of complex **6**, highlighting HCl release during the metalation process.

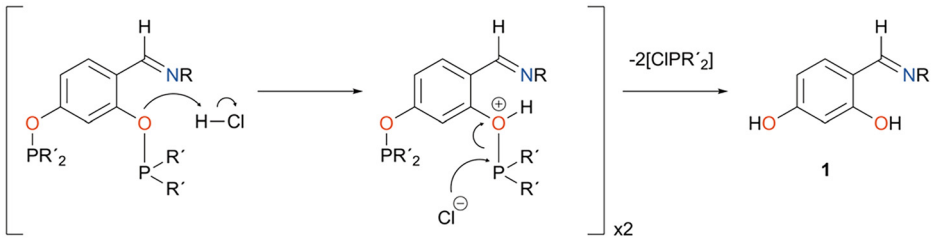

Scheme 6 Proposed HCl-promoted cleavage of the phosphinite P–O bond leading to regeneration of precursor **1** and regeneration of chlorophosphine species.

lents of the corresponding chlorophosphine ($ClPR_2$) into the reaction medium (Scheme 6). Similar acid-promoted cleavage pathways of phosphinite and phosphinite-derived ligands have been documented under halide-rich or acid conditions, supporting the plausibility of this transformation.[61–63]

The liberated chlorophosphine is expected to undergo hydrolysis by adventitious moisture to afford the corresponding phosphinous acid (PR_2OH), a transformation well documented in the literature.[64]

Because starting material **1** cannot undergo further metalation, the remaining $NiCl_2$ instead likely acts as a Lewis acid that coordinates to and activates the iminic nitrogen, generating species 7. This activation facilitates an electrophilic aromatic substitution (EAS) at the C3 position of the aromatic ring to afford σ-adduct **8**, with concomitant loss of aromaticity. Subsequent protonation at nitrogen furnishes intermediate **9**, converting the imine fragment into a better leaving group. Rearrangement is proposed to proceed through a high-energy dearomatized oxonium-type intermediate **10**, in which charge stabilization by the phenolic oxygen enables cleavage of the N-$NiCl_2$ fragment and subsequent rearomatization (Scheme 7).

Addition of the phosphinous acid to the polarized C=C unit in intermediate **10** restores aromaticity, affording intermediate **11**. Subsequent deprotonation of the oxygen atom, followed by oxidation at phosphorus, leads to formation of the observed phosphine oxide-type imine addition complex **12** (Scheme 8). This sequence provides a plausible rationale for the formation of the imine-type addition products and explains the regeneration of aromaticity concomitant with P–C bond formation. Depending on whether Et_3N is present during the metalation step, this pathway may operate either selectively or in competition with alternative processes, resulting in the formation of a single product or a mixture of products.

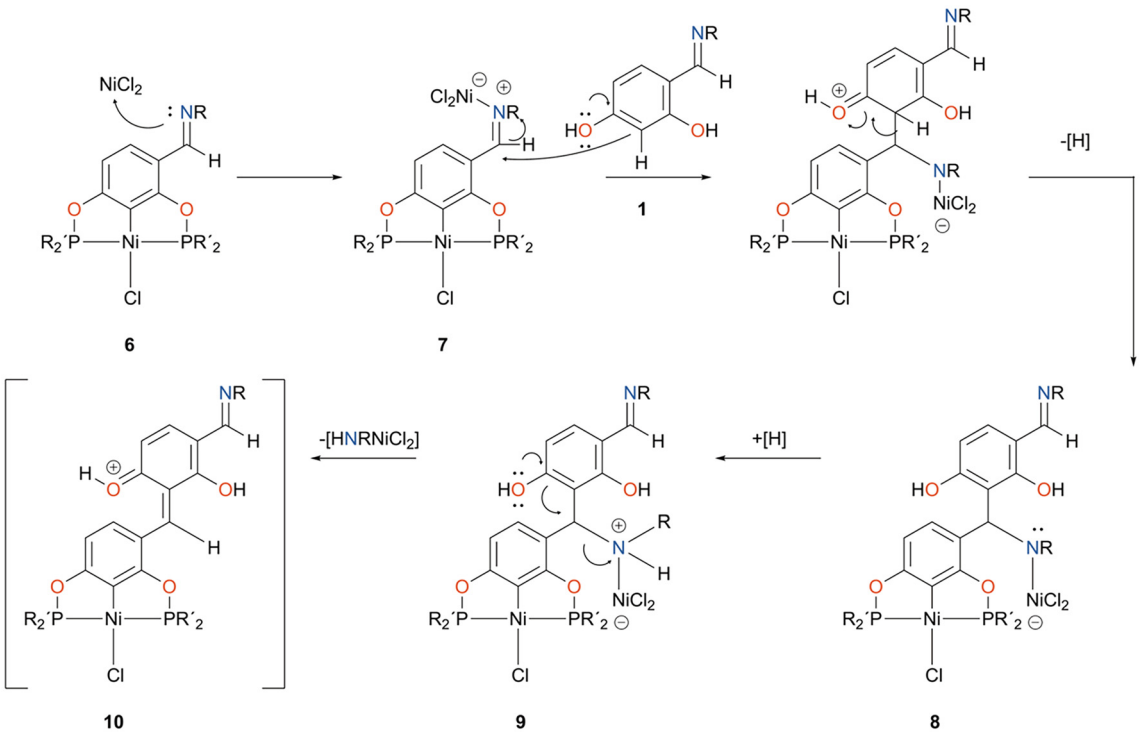

Scheme 7 Proposed Lewis acid-promoted electrophilic aromatic substitution leading to formation of intermediate **10**.

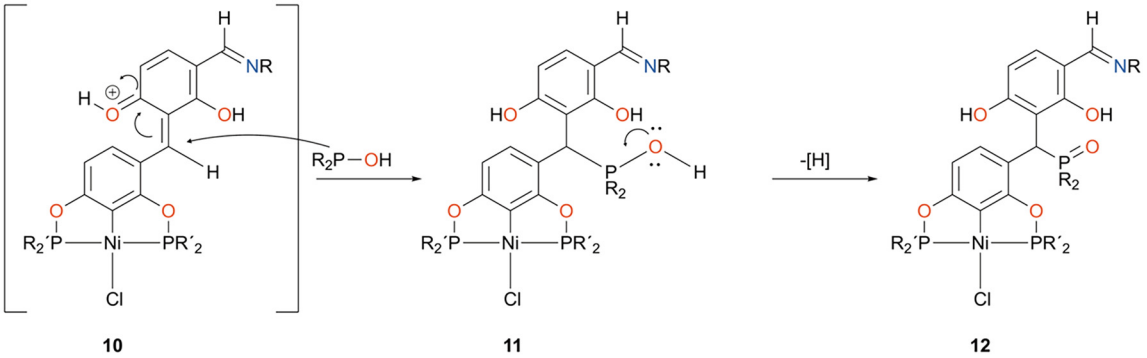

Scheme 8 Proposed addition of phosphinous acid to intermediate **10** leading to formation of the imine-type phosphine oxide addition complex **12** and restoration of aromaticity.

3 X-Ray crystallography

Single crystals suitable for X-ray diffraction of compounds **1b**, **2c**, **3a**, **5b**, and **5c** were obtained under the conditions described in sections 6.1.2 and 6.2.1. Diffraction data were collected at different temperatures depending on the compound: 100 K for **1b**; 130 K for **5b** and **5c**; and 250 K for **2c** and **3a**. All crystal structures were solvent-free, with no solvent molecules present in the crystal lattice. Complex **5b** crystallized in the monoclinic system ($P2_1/n$), compound **1b** crystallized in the orthorhombic system (*Pbca* and $P2_12_12_1$, respectively), while complexes **2c**, **3a**, and **5c** crystallized in the triclinic system ($P\bar{1}$). Detailed crystallographic parameters are provided in Tables S1 and S2.

Compound **1b** was identified as adopting a *trans* iminium-phenolate tautomer, attributable to the influence of the salicylidene moiety, which affects the electronic distribution of the system and shifts the equilibrium from the phenol–imine form to the iminium-phenolate form (Fig. 1).[65] An intramolecular interaction is observed in the iminium-phenolate, consisting of an N1–H1···O1 hydrogen bond that generates an S(6) graph-set motif. This hydrogen-bonding pattern is analogous to that reported for the previously described analogue **1a**.[41] Selected bond lengths and angles are summarized in Table S3.

Aldehyde compound **2c**, the metal center adopts a tetra-coordinate environment with a slightly distorted square planar geometry (Fig. 2). The oxygen atom of the aldehyde group is consistently oriented in the up conformation. Selected bond lengths and angles are summarized in Table S4.

For the addition complexes (**3a**, **5b** and **5c**), the molecular structures are shown in Fig. 3. In all cases, the metal center retains a square-planar geometry, exhibiting only minor distortions relative to their aldehyde precursors. These distortions are primarily reflected in the C–Ni–Cl bond angle, which approaches linearity (≈180°, Table S4) in the isopropyl and *tert*-butyl derivatives, whereas in the phenyl-substituted complexes (**2c** and **5c**) it decreases slightly to approximately 176°. A

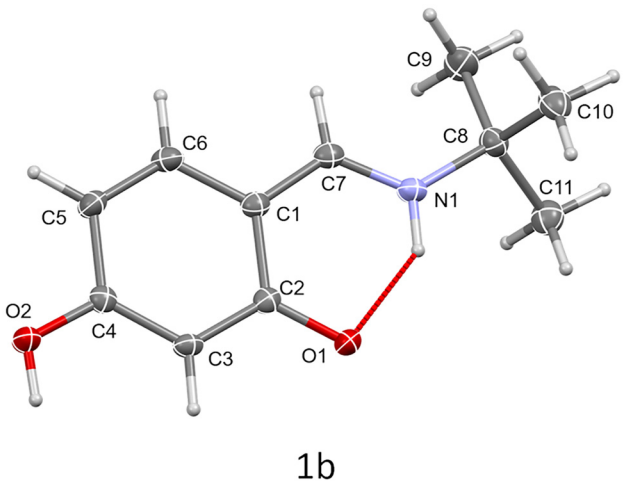

Fig. 1 Molecular structure of compound **1b**. Ellipsoids are represented at 50% of probability. The intramolecular interaction is shown as dashed red lines [an S(6) graph set descriptor].

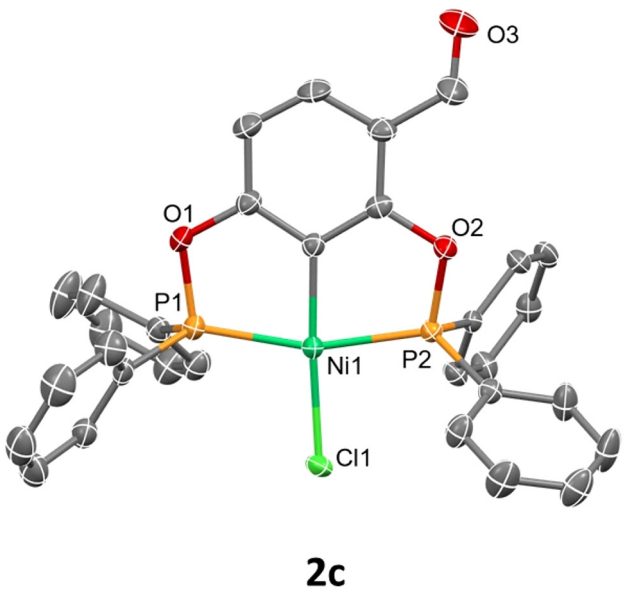

Fig. 2 Molecular structure of compound **2c**. Ellipsoids are presented at 30% probability. The hydrogen atoms were omitted for clarity.

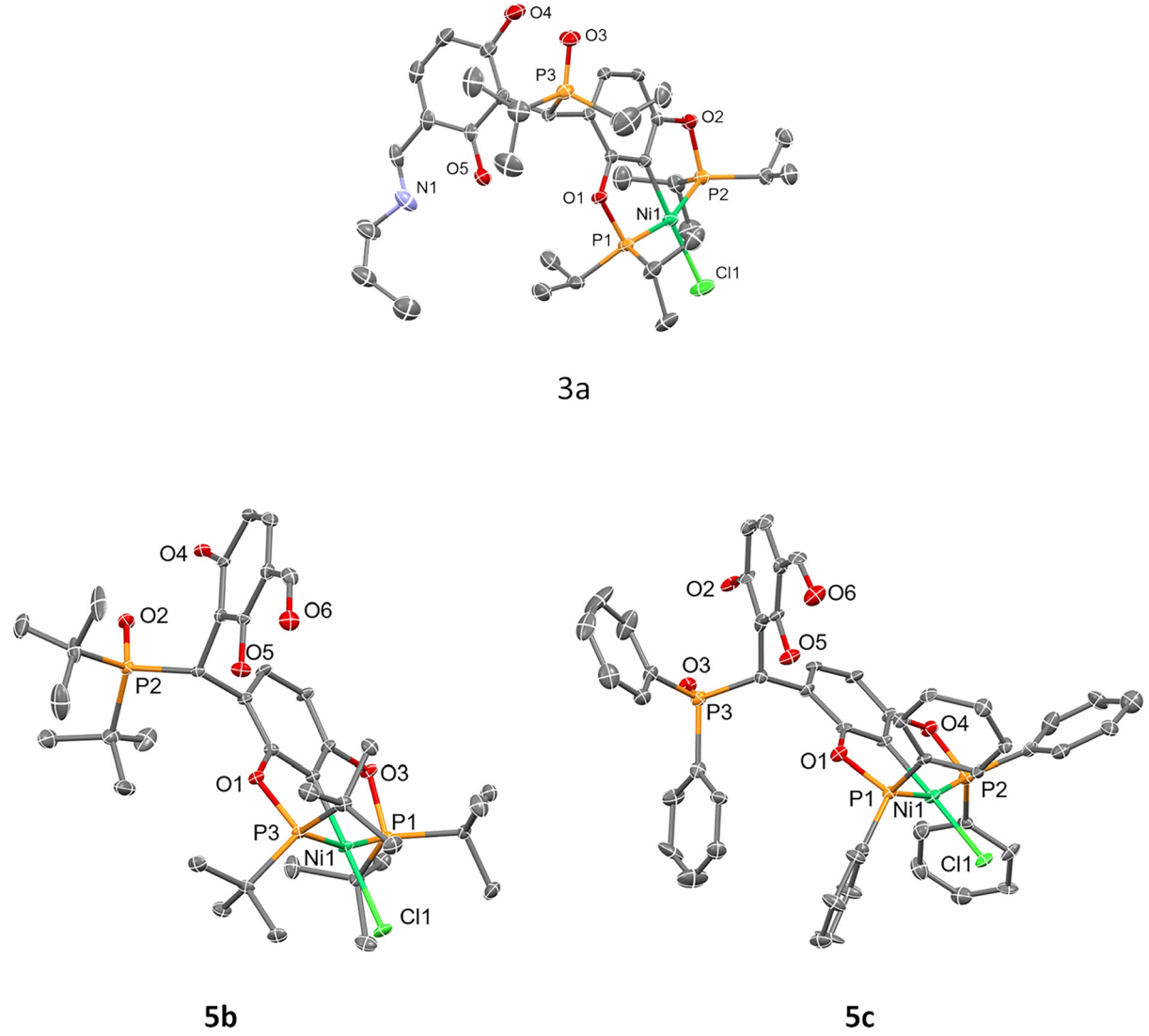

Fig. 3 Molecular structure of compounds **3a** (top) and **5b** and **5c** (bottom). Thermal ellipsoids are drawn at 30% probability. Hydrogen atoms are omitted for clarity.

similar trend is observed for the P–Ni–P angle, which is also reduced in the phenyl derivatives.

Within the molecular frameworks of these four addition complexes, two intramolecular hydrogen-bonding interactions are identified: OH···O=P and OH···N imine, corresponding to S(7) and S(6) graph-set motifs, respectively. The OH···N imine interaction persists in compounds **5b** and **5c**, involving an O5–H5···O6 hydrogen bond within the aldehyde moiety, while retaining the same S(6) graph-set descriptor. In contrast, in compound **5c**, the intramolecular OH···O=P hydrogen bond is no longer observed.

4 Supramolecular analysis

Addition compounds exhibit a wide range of noncovalent intermolecular interactions that play a crucial role in determining their crystal packing and supramolecular organization. These include C–H···O and C–H···Cl hydrogen bonds, as well as C–H···π and π···π stacking contacts, each contributing to the stabilization and dimensionality of the resulting architectures. The prevalence and nature of these interactions are further supported by Hirshfeld surfaces analysis (*vide infra*). A detailed compilation of the most relevant intermolecular contacts is provided in Table S5.

In the case of compound **3a**, the crystal structure reveals a centrosymmetric dimeric motif primarily stabilized by C–H···O hydrogen bonds and π···π stacking interactions. The C–H···O contacts arise from weak hydrogen bonds between propyl C–H donors and phenolic oxygen acceptors, while π···π interactions between adjacent aromatic rings further stabilize the dimeric assembly by reinforcing close intermolecular association (Fig. 4, top).

Aldehyde-type addition complexes further illustrate this structural versatility. Compound **5b** adopts a dimeric supramo-

lecular arrangement, stabilized primarily by C–H···O hydrogen bonds, closely resembling the interaction pattern observed for **3a**. In contrast, **5c** assembles into a centrosymmetric tetrameric motif, predominantly governed by bifurcated C–H···Cl interactions,[66] which promote extended supramolecular connectivity through halogen-assisted hydrogen bonding. These distinct packing modes are depicted in Fig. S51 and S52, respectively.

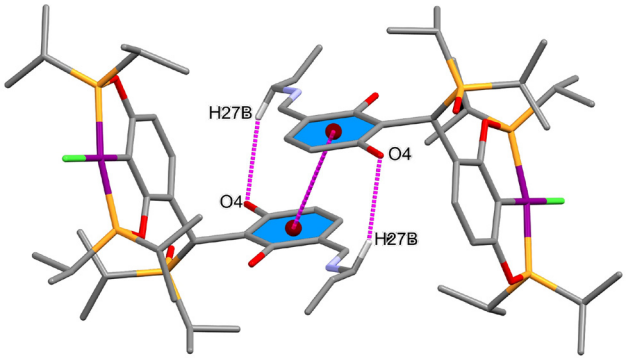

Fig. 4 Fragments of the crystal packing of compounds **3a** highlighting the centrosymmetric dimeric arrangement. Hydrogen atoms not involved in intermolecular interactions are omitted for clarity.

4.1 Hirshfeld surface analysis

The Hirshfeld surface analysis[67] was mapped over the d_{norm} and a shape index functions for the asymmetric unit. In cases where molecular disorder was present, all components were fully included in the analysis. The d_{norm} surfaces display pronounced red regions localized on heteroatoms and selected C–H groups, indicating the presence of short intermolecular contacts relative to the sum of the corresponding van der Waals radii. Complementary red and blue triangular features observed in the shape index maps are characteristic of π···π stacking interactions, which are clearly evident in compound **3a** (Fig. 5).

In addition, the two-dimensional Hirshfeld fingerprint plots,[68,69] reveal clear similarities in the relative contributions of individual intermolecular contacts for compounds **3a**, and **5b**.

A quantitative comparison of contact percentages across the addition complexes (**3a**, **5b** and **5c**) is summarized in Fig. 6. In this representation, compound **5c** exhibits an increased contribution from C···H/H···C interactions, which can be attributed to its higher aromatic content. Notably, in **3a** these contacts

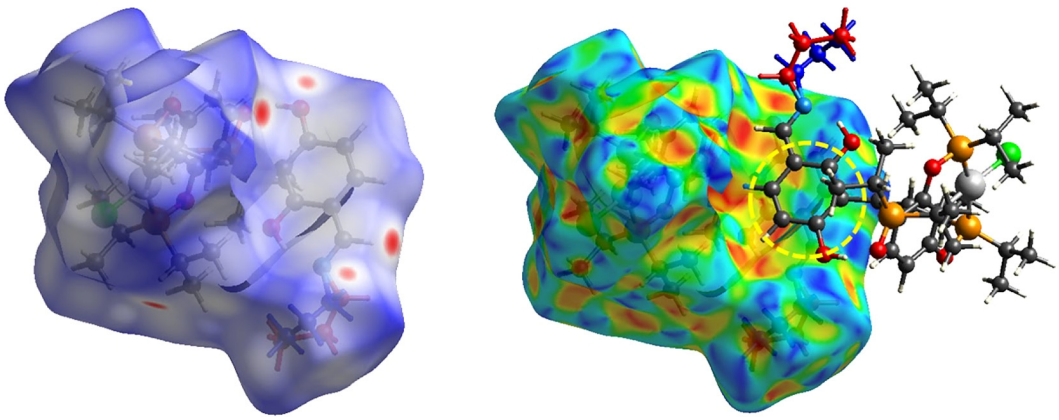

Fig. 5 Hirshfeld surfaces of complex **3a** mapped over the d_{norm} (left) and shape index (right) functions. The yellow dotted circles highlight regions associated with π···π stacking interactions.

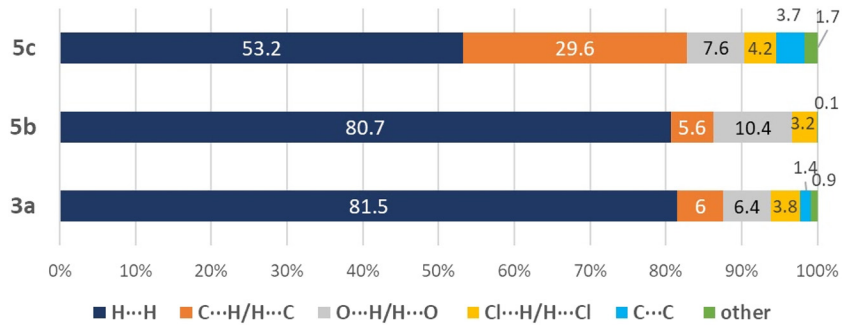

Fig. 6 Individual contribution of contacts in compounds **3a**, **5b** and **5c**.

arise primarily from centrosymmetric π···π stacking interactions.

Additional Hirshfeld surface representations and quantitative fingerprint analyses for compounds **3a**, **5b**, and **5c**, confirming the trends discussed above, are included in the SI (Fig. S53–S57).

5 Conclusions

This study demonstrates that the outcome of Ni–POCOP pincer complex formation is dictated by the presence or absence of a base during the metalation step. When triethylamine is present, the *in situ* generated HCl is efficiently neutralized, suppressing ligand activation pathways and enabling the selective formation of aldehyde-type pincer complexes (**2a–2c**) as single products. In contrast, under base-free conditions, residual acidity promotes phosphinite activation and P–O bond cleavage, leading to the formation of imine-type addition complexes (**3a–4c**) in the reaction mixture, which can partially undergo hydrolysis during chromatographic purification to afford the corresponding aldehyde-type addition complexes (**5a–5c**). Single-crystal X-ray diffraction, complemented by spectroscopic analyses, unequivocally confirms the structures and coordination modes of all isolated species. While Ni–POCOP complexes incorporating imine functionalities have been previously reported, to the best of our knowledge, the formation of addition complexes arising from acid-promoted ligand activation during metalation has not been described, underscoring the critical role of reaction medium acidity in governing the stability and reactivity of phosphinite-based pincer systems.

6 Experimental section

Unless otherwise stated, all reactions were carried out under a nitrogen atmosphere using standard Schlenk techniques. The yields reported correspond to the highest isolated yields obtained under the reaction conditions examined. Toluene was purchased from Tecsiquim and dried according to published procedures (Na^0/acetophenone). Triethylamine was purchased from Sigma-Aldrich and purified according to reported procedures.[70] Column chromatography was performed on silica gel (Merck, 230–400 mesh).

Melting points were recorded on a MELT-TEMP II apparatus and are reported uncorrected. FT-IR spectra were recorden on a Nicolet iS50 (Thermo Fisher Scientific) spectrometer using an attenuated total reflectance (ATR) accesory. ^1H, $^{13}C\{^1H\}$ and $^{31}P\{^1H\}$ NMR spectrum were recorded on a Bruker Ascend 500 MHz spectrometer. Chemical shifts (δ) are reported in ppm and coupling constants (J) in Hz, using TMS or residual solvent signals as internal standards. DMSO-d_6 or $CDCl_3$ were used as deuterated solvents.

Direct analysis in real time ($DART^+$) mass spectrum were recorded on a AccuTOF JMS-T100LC spectrometer. Elemental analyses were performed using a Thermo Scientific Flash 2000 elemental analyzer equipped with a Mettler Toledo XP6 Automated-S microbalance, using sulfanilamide as the calibration standard (Thermo Scientific BN 217826, certified values N = 16.26%, C = 41.81%, H = 4.71%, and S = 18.62%; measured values: N = 16.40%, C = 41.91%, H = 4.65%, and S = 18.63%).

6.1 General synthesis of 4-[(alkylimino)methyl]benzene-1,3-diol (1a–1b, Scheme 2)

Ligands **1a** [41,42] and **1b** [43] were synthesized through a novel methodology, and their characterization data are consistent with the reported values. All reactions were conducted under ambient conditions, without the use of an inert atmosphere. 2,4-Dihydroxibenzaldehyde (**1**; 1 equiv.) was dissolved in ethanol (15 mL) and stirred for 5 minutes. The corresponding amine (**a** or **b**; 1.1 equiv.) was then added dropwise, followed immediately by acetic acid (4 drops). The reaction mixture was refluxed for 10 min, then cooled in an ice/salt bath, and the resulting yellow solid was filtered and washed with cold hexane (3 × 10 mL). The purified products were obtained as crystalline yellow solids and dried under vacuum at 50 °C for 12 h.

6.1.1 Synthesis of 1a. 2,4-Dihydroxibenzaldehyde (**1**; 4 g, 28.9 mmol) and *n*-propylamine (**a**; 1.9 g, 31.8 mmol) were used according to the general procedure (section 6.1). Yield 89% (4.6 g).

6.1.2 Synthesis of 1b. 2,4-Dihydroxibenzaldehyde (**1**; 4 g, 28.9 mmol) and *tert*-butylamine (**b**; 2.3 g, 31.8 mmol) were used according to the general procedure (section 6.1). Yield 91% (5.1 g). Single crystals suitable for X-ray diffraction were obtained by slow diffusion of hexane into a saturated ethanolic solution of the imine at room temperature.

6.2 General synthesis of Ni(II)–POCOP pincer complexes NiCl[3-(CHO)-C_6H_2(2,6-(OPR_2)$_2$)] and Ni(II)–POCOP pincer addition complexes. NiCl{3-[CH(PR_2O)-(4-[(alkylamino/formyl)methyl]benzene-1,3-diol-2-yl)]-C_6H_2(2,6-(OPR_2)$_2$)} (2a–5c, Scheme 3)

Ligand **1a** or **1b** (1 equiv.) was dissolved in toluene (20 mL), and triethylamine (2.1 equiv.) was added dropwise. The resulting mixture was stirred at room temperature for 1 h, after which the corresponding chlorophosphine (a, b, or c; 2 equiv.) was added dropwise and the mixture was stirred for an additional 24 h at room temperature. The resulting mixture was filtered, and the filtrate was added dropwise to a suspension of nickel(II) chloride (1.1 equiv.) in toluene (25 mL). The reaction mixture was then stirred at 110 °C for 24 h.

After cooling to room temperature, the mixture was filtered through Celite®, washing with toluene (3 × 5 mL). The solvent was removed under reduced pressure to afford a yellow solid, which was purified by column chromatography using a polarity gradient. Dichloromethane as eluent to afford the aldehyde-type pincer complexes **2a–2c**, followed by dichloromethane/ethyl acetate (9.5 : 0.5) to obtain the imine-type addition products **3a–4c**, and finally dichloromethane/ethyl

acetate (9 : 1) to afford the aldehyde-type addition products **5a–5c**, when accessible.

Reactions initiated from imine **1a** afforded, depending on the dialkylchlorophosphine employed (chlorodiisopropylphosphine (**a**), di-*tert*-butylchlorophosphine (**b**), or chlorodiphenylphosphine (**c**)), the corresponding complexes **2a**, **3a** and **5a**; **2b**, **3b** and **5b**; or **2c**, **3c** and **5c**, which were isolated sequentially from a single chromatographic column. In contrast, reactions initiated from imine **1b** yielded only the corresponding complexes **2a** and **4a**; **2b** and **4b**; or **2c** and **4c**, which were likewise isolated sequentially from a single chromatographic column.

Due to the low isolated yields of the addition products (**3a–3c**, **4b**, **4c** and **5a–5c**), sufficient material for spectroscopic characterization was obtained by combining the corresponding fractions from multiple independent reactions prior to analysis.

6.2.1 Preparation of complexes 2a–2c, 3a–3c and 5a–5c from ligand 1a

*6.2.1.1 Complexes **2a**, **3a** and **5a**.* Ligand **1a** (926.6 mg, 5.17 mmol), triethylamine (1.51 g, 10.87 mmol), chlorodiisopropylphosphine (**a**; 1.58 g, 10.35 mmol), and anhydrous nickel(II) chloride (737.0 mg, 5.69 mmol) were used according to the general procedure (section 6.2).

6.2.1.1.1Complex **2a**

Yield: 15% (359.5 mg). Anal. calc. for $C_{19}H_{31}ClNiO_3P_2$: C: 49.23, H: 6.74. Found: C: 49.69, H: 6.95. ^{1}H NMR (500 MHz, $CDCl_3$) δ (ppm) 10.15 (s, 1H, OCH), 7.56 (d, $^3J_{H-H}$ = 8.4 Hz, 1H, CH_{Ar}), 6.50 (d, $^3J_{H-H}$ = 8.4 Hz, 1H, CH_{Ar}), 2.56–2.41 (m, 4H, $CH(CH_3)_2$), 1.50–1.31 (m, 24H, $CH(CH_3)_2$). $^{13}C\{^1H\}$ NMR (126 MHz, $CDCl_3$) δ (ppm) 188.47 (OCH), 173.87 (d, $^2J_{C-P}$ = 13.1 Hz, C_{Ar}), 171.39 (d, $^2J_{C-P}$ = 13.6 Hz, C_{Ar}), 128.80 (CH_{Ar}), 126.61 (t, $^2J_{C-P}$ = 21.0 Hz, C_{Ar}), 117.07 (d, $^3J_{C-P}$ = 9.8 Hz, C_{Ar}), 107.26 (d, $^3J_{C-P}$ = 12.0 Hz, CH_{Ar}), 28.08 (d, $^1J_{C-P}$ = 13.9 Hz, $C(CH_3)_3$), 17.55 (d, $^2J_{C-P}$ = 11.0 Hz, $C(CH_3)_3$), 16.82 (d, $^2J_{C-P}$ = 6.0 Hz, $C(CH_3)_3$). $^{31}P\{^1H\}$ NMR (202 MHz, $CDCl_3$) δ (ppm) 193.68 (d, (AB) $^2J_{P-P}$ = 326.2 Hz, 1P), 189.89 (d, (AB) $^2J_{P-P}$ = 326.2 Hz, 1P). M.p. 149 °C. MS-DART: *m*/*z* 463 $[M + 1]^+$ (100%), *m*/*z* 465 $[M + 3]^+$ (72%). FTIR-ATR selected IR data (ν cm^{-1}): 1667 (OCH).

6.2.1.1.2Complex **3a**

Yield: traces. ^{1}H NMR (500 MHz, $CDCl_3$) δ (ppm) 14.51 (s, 1H, OH), 12.38 (s, 1H, OH), 7.91 (s, 1H CH═N), 7.57 (d, $^3J_{H-H}$ = 8.4 Hz, 1H, CH_{Ar}), 6.85 (d, $^3J_{H-H}$ = 8.6 Hz, 1H, CH_{Ar}), 6.28 (d, $^3J_{H-H}$ = 8.4 Hz, 1H, CH_{Ar}), 6.28 (d, $^3J_{H-H}$ = 8.6 Hz, 1H, CH_{Ar}), 5.70 (d, $^2J_{H-P}$ = 10.8 Hz, 1H, $CHP(CH(CH_3)_2)$), 3.51 (diasterotopic, dt, $^2J_{H-H}$ = 12.88 Hz, $^3J_{H-H}$ = 6.58 Hz, 1H, $NCH_2CH_2CH_3$), 3.25 (diasterotopic, dt, $^2J_{H-H}$ = 13.01 Hz, $^3J_{H-H}$ = 6.85 Hz, 1H, $NCH_2CH_2CH_3$), 2.38 (dt, $^2J_{H-P}$ = 14.00 Hz, $^3J_{H-H}$ = 7.16 Hz, 2H, $PCH(CH_3)_2$), 2.31 (q, $^2J_{H-P}$ = 7.14 Hz, $^3J_{H-H}$ = 7.06 Hz, 2H, $PCH(CH_3)_2$), 2.12 (dt, $^2J_{H-P}$ = 14.72 Hz, $^3J_{H-H}$ = 7.31 Hz, 2H, $OPCH(CH_3)_2$), 1.59 (dq, $^3J_{H-H}$ = 13.85 Hz, $^4J_{H-H}$ = 6.93 Hz, 2H, $NCH_2CH_2CH_3$), 1.45–1.02 (m, 36H), 0.91 (t, 3H, $^3J_{H-H}$ = 8.6 Hz, $N(CH_2)_2CH_3$). $^{13}C\{^1H\}$ NMR selected data (126 MHz, $CDCl_3$) δ (ppm) 162.62 (C═N), 131.08 (C_{Ar}), 129.82 (C_{Ar}), 109.46 (C_{Ar}), 109.21 (C_{Ar}), 30.93 (CHP). $^{31}P\{^1H\}$ NMR (202 MHz, $CDCl_3$) δ (ppm) 185.47 (d, (AB) $^2J_{P-P}$ = 324.4 Hz, 1P), 183.40 (d, (AB) $^2J_{P-P}$ = 324.96 Hz, 1P), 66.62 ppm (s, P═O, 1P). M.p. 193 °C. MS-DART: *m*/*z* 758 $[M + 1]^+$ (100%). FTIR-ATR selected IR data (ν cm^{-1}): 1609 (C═N), 1227 (P═O). Single crystals suitable for X-ray diffraction were obtained by slow evaporation from a 1 : 1 CH_2Cl_2/hexane solution.

6.2.1.1.3Complex **5a**

Yield: traces. MS-DART: *m*/*z* 716 $[M + 1]^+$ (100%).

*6.2.1.2 Complexes **2b**, **3b** and **5b**.* Ligand **1a** (926.6 mg, 5.17 mmol), triethylamine (1.51 g, 10.87 mmol), di-*tert*-butylchlorophosphine (**b**; 1.87 g, 10.35 mmol), and anhydrous nickel(II) chloride (737.0 mg, 5.69 mmol) were used according to the general procedure (section 6.2).

6.2.1.2.1Complex **2b**

Yield: 30% (806.0 mg). Anal. calc. for $C_{23}H_{39}ClNiO_3P_2$: C: 53.16, H: 7.57. Found: C: 53.11, H: 7.67. ^{1}H NMR (500 MHz, $CDCl_3$) δ (ppm) 10.19 (s, 1H, OCH), 7.55 (d, $^3J_{H-H}$ = 8.5, 1H, CH_{Ar}), 6.50 (d, $^3J_{H-H}$ = 8.4, 1H, CH_{Ar}), 1.50 (d, $^3J_{H-P}$ = 11.7, 36H, $P(CH(CH_3)_2)$). $^{13}C\{^1H\}$ NMR (126 MHz, $CDCl_3$) δ (ppm) 188.51 (OCH), 174.58 (d, $^2J_{C-P}$ = 11.9, C_{Ar}), 172.02 (d, $^2J_{C-P}$ = 11.8, C_{Ar}), 128.40 (CH_{Ar}), 126.17 (t, $^2J_{C-P}$ = 20.2, C_{Ar}), 116.85 (d, $^3J_{C-P}$ = 9.4, C_{Ar}), 107.09 (d, $^3J_{C-P}$ = 11.4, CH_{Ar}), 39.72 (d, $^1J_{C-P}$ = 9.7, $C(CH_3)_3$), 28.06 (d, $^2J_{C-P}$ = 3.4, $C(CH_3)_3$). $^{31}P\{^1H\}$ NMR (202 MHz, $CDCl_3$) δ (ppm) 196.05 (d, (AB) $^2J_{P-P}$ = 299.9 Hz, 1P), 192.55 (d, (AB) $^2J_{P-P}$ = 300.5 Hz, 1P). M.p. 232 °C. MS-DART *m*/*z* 519 $[M + 1]^+$ (100%), *m*/*z* 521 $[M + 3]^+$ (72%). FTIR-ATR selected IR data (ν cm^{-1}): 1689 (OCH).

6.2.1.2.2Complex **3b**

Yield: traces. ^{1}H NMR (500 MHz, $CDCl_3$) δ (ppm) 14.41 (s, 1H, OH), 13.12 (s, 1H, OH), 7.94 (s, 1H CH═N), 7.92 (d, $^3J_{H-H}$ = 8.6 Hz, 1H, CH_{Ar}), 6.87 (d, $^3J_{H-H}$ = 8.6 Hz, 1H, CH_{Ar}), 6.32 (d, $^3J_{H-H}$ = 8.5 Hz, 2H, CH_{Ar}), 6.00 (d, $^3J_{H-H}$ = 9.4 Hz, 1H, CH_{Ar}), 5.70 (d, $^2J_{H-P}$ = 10.8 Hz, 1H, $P(CH(CH_3)_2)$), 3.54 (diasterotopic, dt, 1H, $^2J_{H-H}$ = 12.9 Hz, $^3J_{H-H}$ = 6.6 Hz, $NCH_2CH_2CH_3$), 3.34 (diasterotopic, dt, 1H, $^2J_{H-H}$ = 12.4 Hz, $^3J_{H-H}$ = 7.2 Hz, $NCH_2CH_2CH_3$), 1.78–1.64 (m, 2H, $NCH_2CH_2CH_3$), 1.63 (dd, 9H, $^3J_{H-P}$ = 11.41 Hz, $^5J_{H-P}$ = 2.68 Hz, $C(CH_3)_3$), 1.47 (dd, 18H, $^3J_{H-P}$ = 11.38 Hz, $^5J_{H-P}$ = 2.62 Hz, $C(CH_3)_3$) 1.42 (dd, 18H, $^3J_{H-P}$ = 11.06 Hz, $^5J_{H-P}$ = 2.68 Hz, $C(CH_3)_3$), 1.28 (d, 9H, $^3J_{H-P}$ = 13.28 Hz, $C(CH_3)_3$), 1.15 (d, 9H, $^3J_{H-P}$ = 13.51 Hz, $C(CH_3)_3$), 0.96 (t, 9H, $^3J_{H-H}$ = 7.39 Hz, $NCH_2CH_2CH_3$). $^{13}C\{^1H\}$ NMR selected data (126 MHz, $CDCl_3$) δ (ppm) 163.29 (C═N), 131.92 (C_{Ar}), 131.47 (C_{Ar}), 111.02 (C_{Ar}), 106.30 (C_{Ar}), 58.13 (diasterotopic, N═$CH_2CH_2CH_3$), 33.11 (d, $^2J_{C-P}$ = 49.00 Hz, $HCPCH(CH_3)_2$), 28.87–26.00 ($C(CH_3)_3$) 24.08 ($CH_2CH_2CH_3$), 14.19 ($CH_2CH_2CH_3$). $^{31}P\{^1H\}$ NMR (202 MHz, $CDCl_3$) δ (ppm) 188.40 (d, (AB) $^2J_{P-P}$ = 301.09 Hz, 1P), 186.49 (d, (AB) $^2J_{P-P}$ = 301.22 Hz, 1P) 74.98 (s, P═O, 1P). M.p. 250 °C. MS-DART: *m*/*z* 842 $[M + 1]^+$ (40%), *m*/*z* 163 $[M\text{-}C_{33}H_{51}ClNNiO_4P_2]$ (100%). FTIR-ATR selected IR data (ν cm^{-1}): 1605 (C═N), 1243 (P═O).

6.2.1.2.3Complex **5b**

Yield: traces. ^{1}H NMR (500 MHz, $CDCl_3$) δ (ppm) 13.91 (s, 1H, OH), 12.61 (s, 1H, OH), 9.57 (s, 1H, OCH), 7.84 (d, 1H, $^3J_{H-H}$ = 8.60 Hz, CH_{Ar}), 7.25 (d, 1H, $^3J_{H-H}$ = 8.59 Hz, CH_{Ar}), 6.55 (d, 1H, $^3J_{H-H}$ = 8.60 Hz, CH_{Ar}), 6.35 (d, 1H, $^3J_{H-H}$ = 8.59 Hz,

CH_{Ar}), 5.81 (d, 1H, $^3J_{H-P}$ = 9.74 Hz, $CHPC(CH_3)_3$), 1.64 (d, 9H, $^3J_{H-P}$ = 13.07 Hz, $PC(CH_3)_3$), 1.49 (d, 9H, $^3J_{H-P}$ = 12.99 Hz, $PC(CH_3)_3$), 1.44 (d, 9H, $^3J_{H-P}$ = 12.79 Hz, $PC(CH_3)_3$), 1.44 (d, 9H, $^3J_{H-P}$ = 12.83 Hz, $PC(CH_3)_3$), 1.30 (d, 9H, $^3J_{H-P}$ = 13.43 Hz, $OPC(CH_3)_3$), 1.17 (d, 9H, $^3J_{H-P}$ = 13.75 Hz, $OPC(CH_3)_3$). $^{13}C\{^1H\}$ NMR selected data (126 MHz, $CDCl_3$) δ (ppm) 193.96 (OCH), 134.16 (CH_{Ar}), 130.87 (CH_{Ar}), 113.49 (CH_{Ar}), 106.30 (CH_{Ar}), 32.00 (d, $^2J_{C-P}$ = 48.43 Hz, $HCPC(CH_3)_3$), 28.39–27.70 (18C, $PC(CH_3)_3$). $^{31}P\{^1H\}$ NMR (202 MHz, $CDCl_3$) δ (ppm) 190.04 (d, (AB) $^2J_{P-P}$ = 301.75 Hz, 1P), 189.96 (d, (AB) $^2J_{P-P}$ = 301.75 Hz, 1P) 74.98 (s, P═O, 1P). MS-DART: *m*/*z* 801 $[M + 1]^+$ (100%). Single crystals suitable for X-ray diffraction were obtained from a 2 : 1 hexane/acetyl acetate solution.

*6.2.1.3 Complexes **2c**, **3c** and **5c**.* Ligand **1a** (926.6 mg, 5.17 mmol), triethylamine (1.51 g, 10.87 mmol), chlorodiphenylphosphine (**c**; 2.28 g, 10.35 mmol), and anhydrous nickel(II) chloride (737.0 mg, 5.69 mmol) were used according to the general procedure (section 6.2).

6.2.1.3.1Complex **2c**

Yield: 3% (93.0 mg). Anal. calc. for $C_{31}H_{23}ClNiO_3P_2$: C: 62.10, H: 3.87. Found: C: 62.02, H: 3.91. ^1H NMR (500 MHz, $CDCl_3$) δ (ppm) 10.30 (s, 1H, OCH), 8.04–7.95 (m, 8H, CH_{Ar}), 7.69 (d, $^3J_{H-H}$ = 8.4, 1H, CH_{Ar}), 7.60–7.51 (m, 4H, CH_{Ar}), 7.54–7.46 (m, 8H, CH_{Ar}), 6.72 (d, $^3J_{H-H}$ = 8.4, 1H, CH_{Ar}). $^{13}C\{^1H\}$ NMR (126 MHz, $CDCl_3$) δ (ppm) 188.26 (OCH), 172.01 (d, $^2J_{C-P}$ = 15.6, C_{Ar}), 169.45 (d, $^2J_{C-P}$ = 16.3, C_{Ar}), 132.33 (d, $^2J_{C-P}$ = 6.4, CH_{Ar}), 132.02 (d, $^2J_{C-P}$ = 12.7, CH_{Ar}), 131.59 (dd, $^1J_{C-P}$ = 7.8, $^3J_{C-P}$ = 4.0, C_{Ar}), 129.88 (CH_{Ar}), 129.12 (d, $^3J_{C-P}$ = 9.9, CH_{Ar}), 127.97 (t, $^2J_{C-P}$ = 23.3, C_{Ar}), 118.08 (d, $^3J_{C-P}$ = 10.9, C_{Ar}), 108.4 (d, $^3J_{C-P}$ = 12.8, CH_{Ar}). $^{31}P\{^1H\}$ NMR (202 MHz, $CDCl_3$) δ (ppm) 148.04 (d, (AB) $^2J_{P-P}$ = 374.2 Hz, 1P), 144.5 (d, (AB) $^2J_{P-P}$ = 374.2 Hz, 1P). M.p. 233 °C. MS-DART *m*/*z* 599 $[M + 1]^+$ (100%), *m*/*z* 601 $[M + 3]^+$ (80%). ATR selected IR data (ν cm^{-1}): 1689 (OCH). Single crystals suitable for X-ray diffraction were obtained by slow diffusion of MeOH into a saturated CH_2Cl_2 solution of the complex at room temperature.

6.2.1.3.2Complex **3c**

Yield: traces. ^1H NMR (500 MHz, $CDCl_3$) δ (ppm) 12.90 (s, 1H, OH), 12.52 (s, 1H, OH), 9.50 (s, 1H CH═N), 8.02–7.93 (m, 13H, CH_{Ar}), 7.60–7.17 (m, 19H, CH_{Ar}), 6.59 (d, $^3J_{H-H}$ = 8.5 Hz, 1H, CH_{Ar}), 6.51 (d, $^3J_{H-H}$ = 8.6 Hz, 1H, CH_{Ar}), 6.23 (d, $^2J_{H-P}$ = 12.7 Hz, 1H, PPh_2). $^{13}C\{^1H\}$ NMR selected data (126 MHz, $CDCl_3$) δ (ppm) 194.09 (C═N), 132.48–130.90 (C_{Ar}), 129.04–128.60 (C_{Ar}), 128.11 (C_{Ar}). $^{31}P\{^1H\}$ NMR (202 MHz, $CDCl_3$) δ (ppm) 141.3 (s, AB, 2P), 42.3 (s, P═O, 1P). M.p. 258 °C. MS-DART: *m*/*z* 961 $[M + 1]^+$ (8%), *m*/*z* 203 $[M\text{-}C_{41}H_{35}ClNNiO_4P_2]$ (100%). FTIR-ATR selected IR data (ν cm^{-1}): 1601 (C═N), 1233 (P═O).

6.2.1.3.3Complex **5c**

Yield: traces. ^1H NMR (500 MHz, $CDCl_3$) δ (ppm) 14.52 (s, 1H, OH), 12.31 (s, 1H, OH), 8.01–7.82 (m, 13H, CH_{Ar}), 7.56–7.32 (m, 16H, CH_{Ar}), 6.82 (d, 1H, $^3J_{H-H}$ = 8.73 Hz, CH_{Ar}), 6.71 (m, 2H, CH_{Ar}), 6.58 (m, 2H, CH_{Ar}), 6.26 (d, 1H, $^3J_{H-H}$ = 8.66 Hz, CH_{Ar}). $^{13}C\{^1H\}$ NMR selected data (126 MHz, $CDCl_3$) δ (ppm) 194.09 (C═O), 133.48–127.63 (C_{Ar}), 115.26–107.38 (C_{Ar}), $^{31}P\{^1H\}$ NMR (202 MHz, $CDCl_3$) δ (ppm) 141.28 (d, (AB) $^2J_{P-P}$ = 372.29 Hz, 1P), 139.21 (d, (AB) $^2J_{P-P}$ = 372.02 Hz, 1P), 42.88 (s, P═O, 1P). Single crystals suitable for X-ray diffraction were obtained from a 2 : 1 hexane/acetyl acetate solution.

6.2.2 Preparation of complexes 2a–2c and 4a–4c from ligand 1b

*6.2.2.1 Complexes **2a** and **4a**.* Ligand **1b** (1 g, 5.17 mmol), triethylamine (1.51 g, 10.87 mmol), chlorodiisopropylphosphine (**a**; 1.58 g, 10.35 mmol), and anhydrous nickel(II) chloride (737.0 mg, 5.69 mmol) were used according to the general procedure (section 6.2).

6.2.2.1.1Complex **2a**

Yield: 22% (527.2 mg).

6.2.2.1.2Complex **4a**

Yield: 53% (2.1 g). Anal. calc. for $C_{36}H_{59}ClNNiO_5P_3$: C: 55.94, H: 7.69, N: 1.81. Found: C: 56.00, H: 7.81, N: 1.92. ^1H NMR (500 MHz, $CDCl_3$) δ (ppm) 15.06 (s, 1H, OH), 12.47 (s, 1H, OH), 7.95 (s, 1H, CH═N), 7.60 (d, $^3J_{H-H}$ = 8.5 Hz, 1H, CH_{Ar}), 6.90 (d, $^3J_{H-H}$ = 8.7 Hz, 1H, CH_{Ar}), 6.35 (d, $^3J_{H-H}$ = 8.4 Hz, 1H, CH_{Ar}), 6.29 (d, $^3J_{H-H}$ = 8.7 Hz, 1H, CH_{Ar}), 5.82 (d, $^2J_{H-P}$ = 10.7 Hz, 1H, CHP), 2.51–2.40 (m, 2H), 2.41–2.32 (m, 2H), 2.26–2.12 (m, 4H), 1.52–1.11 (m, 45H) ppm. $^{13}C\{^1H\}$ NMR selected data (126 MHz, $CDCl_3$) δ (ppm) 158.14 (C═N), 130.72 (C_{Ar}), 110.05 (C_{Ar}), 110.03 (C_{Ar}), 106.39 (C_{Ar}), 30.95 (CHP), 28.28–27.4 (4C, CH), 25.79–25.37 (2C, CH). $^{31}P\{^1H\}$ NMR (202 MHz, $CDCl_3$) δ (ppm) 185.30 (d, (AB) $^2J_{P-P}$ = 324.7 Hz, 1P), 183.18 (d, (AB) $^2J_{P-P}$ = 324.8 Hz, 1P), 66.60 ppm (s, P═O, 1P). M.p. 231 °C. MS-DART: *m*/*z* 771 $[M + 1]^+$ (100%). FTIR-ATR selected IR data (ν cm^{-1}): 1603 (C═N), 1242 (P═O).

*6.2.2.2 Complexes **2b** and **4b**.* Ligand **1b** (1 g, 5.17 mmol), triethylamine (1.51 g, 10.87 mmol), di-*tert*-butylchlorophosphine (**b**; 1.87 g, 10.35 mmol), and anhydrous nickel(II) chloride (737.0 mg, 5.69 mmol) were used according to the general procedure (section 6.2).

6.2.2.2.1Complex **2b**

Yield: 37% (994.0 mg).

6.2.2.2.2Complex **4b**

Yield: traces. ^1H NMR (500 MHz, $CDCl_3$) δ (ppm) 13.02 (s, 1H, OH), 11.40 (s, 1H, OH), 9.67 (s, 1H, CH═N), 7.91 (d, $^3J_{H-H}$ = 9.0 Hz, 1H, CH_{Ar}), 7.37 (d, $^3J_{H-H}$ = 8.5 Hz, 1H, CH_{Ar}), 6.85 (d, $^3J_{H-H}$ = 8.7 Hz, 1H, CH_{Ar}), 6.32 (d, $^3J_{H-H}$ = 8.6 Hz, 1H, CH_{Ar}), 6.06 (d, $^2J_{H-P}$ = 9.2 Hz, 1H, CHP), 1.63 (d, $^3J_{H-H}$ = 12.9 Hz, 12H), 1.46 (d, $^3J_{H-H}$ = 12.7 Hz, 24H), 1.42 (d, $^3J_{H-H}$ = 12.5 Hz, 12H), 1.15 (d, $^3J_{H-H}$ = 13.6 Hz, 12H) ppm. $^{13}C\{^1H\}$ NMR (126 MHz, $CDCl_3$) δ (ppm) 194.3 (C═N), 132.35 (C_{Ar}), 136.87 (C_{Ar}), 133.48 (C_{Ar}), 111.89 (C_{Ar}), 33.44 (CHP), 30.16–27.93 (6C, CH_3). $^{31}P\{^1H\}$ NMR (202 MHz, $CDCl_3$) δ (ppm) 189.07 (d, (AB) $^2J_{P-P}$ = 301.5 Hz, 1P), 186.10 (d, (AB) $^2J_{P-P}$ = 302.01 Hz, 1P), 76.43 ppm (s, P═O, 1P). MS-DART: *m*/*z* 858 $[M + 1]^+$.

*6.2.2.3 Complexes **2c** and **4c**.* Ligand **1b** (1 g, 5.17 mmol), triethylamine (1.51 g, 10.87 mmol), chlorodiphenylphosphine (**c**; 2.28 g, 10.35 mmol), and anhydrous nickel(II) chloride (737.0 mg, 5.69 mmol) were used according to the general procedure (section 6.2).

6.2.2.3.1Complex **2c**

Yield: 11% (341.0 mg).

6.2.2.3.2Complex **4c**

Yield: traces. ^{1}H NMR (500 MHz, $CDCl_3$) δ (ppm) 14.60 (s, 1H, OH), 12.30 (s, 1H, OH), 7.80 (s, 1H, CH═N), 7.98–7.80 (m, 10H, CH_{Ar}), 7.54–7.34 (m, 14H, CH_{Ar}), 7.23 (m, 2H, CH_{Ar}), 7.05 (m, 1H, CH_{Ar}), 6.82 (d, $^{3}J_{H-H}$ = 8.69 Hz, 1H, CH_{Ar}), 6.73 (m, 2H, CH_{Ar}), 6.58 (m, 2H, CH_{Ar}), 6.22 (d, $^{3}J_{H-H}$ = 8.71 Hz, 1H, CH_{Ar}), 1.36 (s, 9H, $C(CH_3)_3$). $^{13}C\{^{1}H\}$ NMR (126 MHz, $CDCl_3$) δ (ppm) 158.0 (C═N), 133.82–127.64 (C_{Ar}), 110.33 (C_{Ar}), 108.04 (C_{Ar}), 111.89 (C_{Ar}), 35.45 (CHP), 29.90 (3C, CH_3). $^{31}P\{^{1}H\}$ NMR (202 MHz, $CDCl_3$) δ (ppm) 140.20 (s, (AB), 1P), 140.06 (s, (AB), 1P), 43.23 ppm (s, P═O, 1P). MS-DART: m/z 976 $[M-1]^{+}$.

6.3 General synthesis of Ni(II)–POCOP pincer complexes. NiCl[3-(CHO)-C_6H_2(2,6-$(OPR_2)_2$)] (2a–2c, Scheme 4)

Ligand **1a** or **1b** (1 equiv.) was dissolved in toluene (20 mL), and triethylamine (2.1 equiv.) was added dropwise. The corresponding dialkylchlorophosphine (**a**, **b**, or **c**; 2 equiv.) was then added dropwise, and the reaction mixture was stirred at room temperature for 6 h. The resulting mixture was filtered, and the filtrate was added dropwise to a suspension of nickel(II) chloride (1.1 equiv.) in toluene (25 mL). Subsequently, triethylamine (1.2 equiv.) was added, and the mixture was stirred at 110 °C for 18 h. After cooling to room temperature, the mixture was filtered through Celite®, washing with toluene (3 × 5 mL). The solvent was removed under reduced pressure to afford a yellow solid, which was purified by column chromatography using dichloromethane as eluent.

6.3.1 Preparation of complexes 2a–2c from ligand 1a

*6.3.1.1 Complex **2a**.* Ligand **1a** (926.6 mg, 5.17 mmol), triethylamine (first addition: 1.51 g, 10.87 mmol; second addition: 627.4 mg, 6.20 mmol), chlorodiisopropylphosphine (**a**; 1.58 g, 10.35 mmol), and anhydrous nickel(II) chloride (737.0 mg, 5.69 mmol) were used according to the general procedure (section 6.3). Yield: 23% (551.2 mg).

*6.3.1.2 Complex **2b**.* Ligand **1a** (926.6 mg, 5.17 mmol), triethylamine (first addition: 1.51 g, 10.87 mmol; second addition: 627.4 mg, 6.20 mmol), di-*tert*-butylchlorophosphine (**b**; 1.87 g, 10.35 mmol), and anhydrous nickel(II) chloride (737.0 mg, 5.69 mmol) were used according to the general procedure (section 6.3). Yield: 30% (806.0 mg).

*6.3.1.3 Complex **2c**.* Ligand **1a** (926.6 mg, 5.17 mmol), triethylamine (first addition: 1.51 g, 10.87 mmol; second addition: 627.4 mg, 6.20 mmol), chlorodiphenylphosphine (**c**; 2.28 g, 10.35 mmol), and anhydrous nickel(II) chloride (737.0 mg, 5.69 mmol) were used according to the general procedure (section 6.3). Yield: 5% (155.0 mg).

6.3.2 Preparation of complexes 2a–2c from ligand 1b

*6.3.2.1 Complex **2a**.* Ligand **1b** (1 g, 5.17 mmol), triethylamine (first addition: 1.51 g, 10.87 mmol; second addition: 627.4 mg, 6.20 mmol), chlorodiisopropylphosphine (**a**; 1.58 g, 10.35 mmol), and anhydrous nickel(II) chloride (737.0 mg, 5.69 mmol) were used according to the general procedure (section 6.3). Yield: 63% (1.5 g).

*6.3.2.2 Complex **2b**.* Ligand **1b** (1 g, 5.17 mmol), triethylamine (first addition: 1.51 g, 10.87 mmol; second addition: 627.4 mg, 6.20 mmol), di-*tert*-butylchlorophosphine (**b**; 1.87 g, 10.35 mmol), and anhydrous nickel(II) chloride (737.0 mg, 5.69 mmol) were used according to the general procedure (section 6.3). Yield 80% (2.1 g).

*6.3.2.3 Complex **2c**.* Ligand **1b** (1 g, 5.17 mmol), triethylamine (first addition: 1.51 g, 10.87 mmol; second addition: 627.4 mg, 6.20 mmol), chlorodiphenylphosphine (**c**; 2.28 g, 10.35 mmol), and anhydrous nickel(II) chloride (737.0 mg, 5.69 mmol) were used according to the general procedure (section 6.3). Yield 55% (1.7 g).

6.4 Data collection and refinement for compounds 1b (CCDC 2515386), 2c (CCDC 2515382), 3a (CCDC 2529829), 5b (CCDC 2515642) and 5c (CCDC 2515643)

Complex **3a** was characterized on a Bruker D8 Venture diffractometer equipped with a Mo-Kα X-ray source (A = 0.71073 Å). Cell parameters were determined using the Bruker SAINT. The rest of the crystals were mounted on a Bruker Smart Apex II diffractometer equipped with a Mo-target X-Ray source (λ = 0.71073 Å). The detector was placed at 5.0 cm from the crystals, and frames were collected with a scan width of 0.5 cm in ω and an exposure time of 10 s per frame. Data were integrated with the Bruker SAINT software using a narrow-frame integration algorithm. Hydrogen atoms were input at calculated positions and allowed to ride on the atoms to which they were attached. Absorption corrections were applied using the SADABS program.[71] Complex **5b** and **5c** were characterized on an Oxford Diffraction Gemini diffractometer equipped with a Mo-Kα X-ray source (λ = 0.71073 Å). CrysAlisPro and CrysAlis RED software packages were used for data collection and integration.[72] Structure solutions and refinements were carried out with the SHELXS-2018 and SHELXL-2019 packages.[73,74]

Molecular structures were visualised, drawn, and intermolecular distances in the crystal structures of compounds were analysed with Mercury[75] Software V2023.3.0. Hirshfeld surfaces and fingerprints plots were computed by each of the molecules of the asymmetric unit with CrystalExplorer[76] V21.5.

Author contributions

Synthesis: J. R.-G. and J. S. O.-O.; writing – original draft: J. R.-G. and T. K. H.; X-ray and supramolecular analyses: A. A.-C., S. H.-O., M. F.-A., and J. R.-G.; visualization: J. R.-G., A. R.-M. and J. S. S.-G. review and editing: J. R.-G., T. K. H., and D. M.-M.; conceptualization and supervision, review and editing, funding acquisition: D. M.-M.

Conflicts of interest

The authors declare no conflict of interest.

Data availability

The data supporting this article is included in the supporting information and contains NMR, FTIR and Mass spectra.

Crystallographic data for compounds **2c**, **1b**, **5b**, **5c** and **3a** have been deposited at the Cambridge Crystallographic Data Centre (CCDC 2515382, 2515386, 2515642, 2515643 and 2529829) and can be obtained free of charge *via* https://www.ccdc.cam.ac.uk/structures. See DOI: https://doi.org/10.1039/d6dt00442c.

CCDC 2515382 (**2c**), 2515386 (**1b**), 2515642 (**5b**), 2515643 (**5c**) and 2529829 (**3a**) contain the supplementary crystallographic data for this paper.[77a–e]

Acknowledgements

J. R.-G. gratefully acknowledges Dr T. Keith Hollis (Department of Chemistry, Mississippi State University) for insightful discussions, valuable assistance during the preparation of the manuscript, and, in particular, for his kind advice and friendship. J. R.-G. also acknowledges CONAHCyT for the Doctoral Fellowship (CVU 1099979). A. A.-C. expresses gratitude to CONAHCyT for the postdoctoral fellowships awarded under the "Estancias Posdoctorales por México 2022(1)" program. D. M.-M. would like to thank UNAM-DGAPA-PAPIIT IN223323 and CONAHCYT A1-S-033933 for their generous financial support.

References

1 *The Privileged Pincer-Metal Platform: Coordination Chemistry & Applications*, ed. G. van Koten and R. A. Gossage, Springer, Cham, 2016.
2 M. Albrecht and M. M. Lindner, *Dalton Trans.*, 2011, **40**, 8733–8744.
3 M. Vogt and R. Langer, *Eur. J. Inorg. Chem.*, 2020, **2020**, 3885–3898.
4 E. Peris and R. H. Crabtree, *Chem. Soc. Rev.*, 2018, **47**, 1959–1968.
5 C. J. Moulton and B. L. Shaw, *J. Chem. Soc., Dalton Trans.*, 1976, 1020–1024.
6 G. van Koten, K. Timmer, J. G. Noltes and A. L. Spek, *J. Chem. Soc., Chem. Commun.*, 1978, 250–252.
7 F. Fang, J. X. Kang, C. Q. Xu, J. Chang, J. Zhang, S. Li and X. Chen, *Inorg. Chem.*, 2021, **60**, 18924–18937.
8 H. Valdés, M. A. García-Eleno, D. Canseco-Gonzalez and D. Morales-Morales, *ChemCatChem*, 2018, **10**, 3136–3172.
9 M. Rauch, S. Kar, A. Kumar, L. Avram, L. J. W. Shimon and D. Milstein, *J. Am. Chem. Soc.*, 2020, **142**, 14513–14521.
10 M. Mastalir, M. Glatz, N. Gorgas, B. Stöger, E. Pittenauer, G. Allmaier, L. F. Veiros and K. Kirchner, *Chem. – Eur. J.*, 2016, **22**, 12316–12320.
11 M. Albrecht and G. van Koten, *Angew. Chem., Int. Ed.*, 2001, **40**, 3750–3781.
12 H. Valdés, E. Rufino-Felipe and D. Morales-Morales, *J. Organomet. Chem.*, 2019, **898**, 120864.
13 M. A. Mohite and M. S. Balakrishna, *Catal. Sci. Technol.*, 2025, **15**, 5713–5723.
14 J. Ruiz-Galindo, A. Amaya-Flórez, J. S. Serrano-García and D. Morales-Morales, *An. Quim.*, 2025, **121**, 137.
15 A. Amaya-Flórez, J. R.-Galindo, E. Sanchez-Yocue, A. Ruiz-Martinez, J. S. Serrano-García, A. Romo-Pérez, P. Cano-Sanchez, V. Reyes-Marquez, R. Le Lagadec and D. Morales-Morales, *RSC Med. Chem.*, 2025, **16**, 5125–5195.
16 M. Asay and D. Morales-Morales, *Dalton Trans.*, 2015, **44**, 17432–17447.
17 A. Avila-Sorrosa, H. A. Jiménez-Vázquez, A. Reyes-Arellano, J. R. Pioquinto-Mendoza, R. A. Toscano, L. González-Sebastián and D. Morales-Morales, *J. Organomet. Chem.*, 2016, **819**, 69–75.
18 Z. N. Gafurov, A. O. Kantyukov, A. A. Kagilev, A. A. Kagileva, I. F. Sakhapov, I. K. Mikhailov and D. G. Yakhvarov, *Molecules*, 2021, **26**, 4063.
19 J. S. Serrano-García, A. Amaya-Flórez, J. R.-Galindo, L. González-Sebastián, L. H. Delgado-Rangel and D. Morales-Morales, *Inorganics*, 2024, **12**, 221.
20 V. A. Kozlov, D. V. Aleksanyan, Y. V. Nelyubina, K. A. Lyssenko, P. V. Petrovskii, A. A. Vasil'ev and I. L. Odinets, *Organometallics*, 2011, **30**, 2920–2932.
21 I. K. Mikhailov, Z. N. Gafurov, A. A. Kagilev, A. O. Kantyukov, I. F. Sakhapov, E. M. Zueva, A. A. Zagidullin, O. G. Sinyashin and D. G. Yakhvarov, *Russ. J. Coord. Chem.*, 2025, **51**, 430–437.
22 A. Naghipour, S. J. Sabounchei, D. Morales-Morales, S. Hernández-Ortega and C. M. Jensen, *J. Organomet. Chem.*, 2004, **689**, 2494–2502.
23 K. Talukdar, A. Issa and J. W. Jurss, *Front. Chem.*, 2019, **7**, 451520.
24 O. V. Ozerov, C. Guo and B. M. Foxman, *J. Organomet. Chem.*, 2006, **691**, 4802–4806.
25 J. M. Serrano-Becerra, S. Hernández-Ortega and D. Morales-Morales, *Inorg. Chim. Acta*, 2010, **363**, 1306–1310.
26 M. R. Eberhard, S. Matsukawa, Y. Yamamoto and C. M. Jensen, *J. Organomet. Chem.*, 2003, **687**, 185–189.
27 R. Favela-Mendoza, E. Rufino-Felipe, H. Valdés, R. A. Toscano, S. Hernandez-Ortega and D. Morales-Morales, *Inorg. Chim. Acta*, 2020, **512**, 119920.
28 Z. Wang, M. R. Eberhard, C. M. Jensen, S. Matsukawa and Y. Yamamoto, *J. Organomet. Chem.*, 2003, **681**, 189–195.
29 H. A. Younus, N. Ahmad, W. Su and F. Verpoort, *Coord. Chem. Rev.*, 2014, **276**, 112–152.
30 M. E. O'Reilly and A. S. Veige, *Chem. Soc. Rev.*, 2014, **43**, 6325–6369.
31 M. S. S. Adam, O. M. El-Hady and F. Ullah, *RSC Adv.*, 2019, **9**, 34311–34329.
32 D. A. Valyaev, J. Willot, L. P. Mangin, D. Zargarian and N. Lugan, *Dalton Trans.*, 2017, **46**, 10193–10196.
33 M. Camacho-Espinoza, A. Reyes-Deloso, R. A. Toscano, J. G. Penieres-Carrillo, J. G. López-Cortés, M. C. Ortega-Alfaro and F. Ortega-Jiménez, *New J. Chem.*, 2019, **43**, 12967–12978.
34 M. A. Solano-Prado, F. Estudiante-Negrete and D. Morales-Morales, *Polyhedron*, 2010, **29**, 592–600.

35 E. G. Morales-Espinoza, R. Coronel-García, H. Valdés, R. Reyes-Martínez, J. M. German-Acacio, B. A. Aguilar-Castillo, R. A. Toscano, N. Ortiz-Pastrana and D. Morales-Morales, *J. Organomet. Chem.*, 2018, **867**, 155–160.
36 A. A. Castillo-García, L. González-Sebastián, L. Lomas-Romero, S. Hernandez-Ortega, R. A. Toscano and D. Morales-Morales, *New J. Chem.*, 2021, **45**, 10204–10216.
37 J. A. Rosas-Ortiz, J. R. Pioquinto-Mendoza, L. González-Sebastián, S. Hernandez-Ortega, M. Flores-Alamo and D. Morales-Morales, *Eur. J. Inorg. Chem.*, 2021, **2021**, 2452–2463.
38 A. Aragón-Muriel, B. A. Aguilar-Castillo, E. Rufino-Felipe, H. Valdés, L. González-Sebastián, R. N. Osorio-Yáñez, Y. Liscano, V. Gómez-Benítez, D. Polo-Cerón and D. Morales-Morales, *Polyhedron*, 2022, **227**, 116115.
39 M. A. Roque-Ramires, L. Shen and R. Le Lagadec, *Eur. J. Inorg. Chem.*, 2020, **2020**, 2700–2708.
40 A. Amaya-Flórez, J. S. Serrano-García, J. Ruiz-Galindo, A. Arenaza-Corona, S. Hernández-Ortega, A. L. Orjuela, J. Alí-Torres, M. Flores-Alamo, V. Reyes-Márquez and D. Morales-Morales, *New J. Chem.*, 2025, **49**, 5173–5186.
41 J. S. Rafelt, J. H. Clark, D. J. Macquarrie and C. Boxwell, *J. Chem. Res.*, 2000, **2000**, 564–565.
42 A. Trerotola, G. Gravina, V. Vykhovanets, N. Blal, D. Guarnieri, A. Maranzana, M. Lamberti, M. Mazzeo and M. Strianese, *J. Inorg. Biochem.*, 2025, **267**, 112875.
43 R. W. Chesnut, R. R. Cesati, C. S. Cutler, S. L. Pluth and J. A. Katzenellenbogen, *Organometallics*, 1998, **17**, 4889–4896.
44 C. A. Tolman, *Chem. Rev.*, 1977, **77**, 313–348.
45 T. M. Porter, A. L. Ostericher and C. P. Kubiak, *Chem. Sci.*, 2019, **10**, 7907–7912.
46 D. J. M. Snelders, G. van Koten and R. J. M. Klein Gebbink, *Chem. – Eur. J.*, 2011, **17**, 42–57.
47 H. Clavier and S. P. Nolan, *Chem. Commun.*, 2010, **46**, 841.
48 M. P. Mitoraj and A. Michalak, *Inorg. Chem.*, 2010, **49**, 578–582.
49 R. H. Crabtree, *The Organometallic Chemistry of the Transition Metals*, Wiley, Hoboken, NJ, 6th edn, 2014.
50 U. Nettekoven, M. Widhalm, H. Kalchhauser, P. C. J. Kamer, P. W. N. M. van Leeuwen, M. Lutz and A. L. Spek, *J. Org. Chem.*, 2001, **66**, 759–770.
51 R. W. Taft, *J. Am. Chem. Soc.*, 1952, **74**, 2729–2732.
52 L. P. Hammett, *J. Am. Chem. Soc.*, 1937, **59**, 96–103.
53 *The Chemistry of Pincer Compounds*, ed. D. Morales-Morales and C. M. Jensen, Elsevier, Amsterdam, 2007.
54 *Organometallic Pincer Chemistry*, ed. G. van Koten and D. Milstein, Springer, Berlin, 2013.
55 *Pincer and Pincer-Type Complexes: Applications in Organic Synthesis and Catalysis*, ed. K. J. Szabó and O. F. Wendt, Wiley, Weinheim, 2014.
56 T. M. Hood and A. B. Chaplin, *Dalton Trans.*, 2021, **50**, 2472–2482.
57 P. S. Pregosin, *NMR in Organometallic Chemistry*, Wiley-VCH, Weinheim, 2013.
58 H. Günther, *NMR Spectroscopy : Basic principles, Concepts and Applications in Chemistry*, Wiley-VCH, Weinheim, 2013.
59 A. D. Bain, *Prog. Nucl. Magn. Reson. Spectrosc.*, 2003, **43**, 63–103.
60 O. Kühl, *Phosphorus-31 NMR Spectroscopy*, Springer, Berlin, 2009.
61 H. R. Hudson and J. C. Roberts, *J. Chem. Soc., Perkin Trans. 2*, 1974, 1575.
62 P. S. Khokhlov, *Russ. Chem. Rev.*, 1984, **53**, 463–475.
63 F. Chaux, S. Frynas, H. Laureano, C. Salomon, G. Morata, M.-L. Auclair, M. (Massoud) Stephan, R. Merdès, P. Richard, M.-J. Ondel-Eymin, J.-C. Henry, J. Bayardon, C. Darcel and S. Jugé, *C. R. Chim.*, 2010, **13**, 1213–1226.
64 T. I. Mulashkina, A. M. Kulakova and M. G. Khrenova, *J. Chem. Inf. Model.*, 2025, **65**, 8181–8193.
65 S. D. Chatziefthimiou, Y. G. Lazarou, E. Hadjoudis, T. Dziembowska and I. M. Mavridis, *J. Phys. Chem. B*, 2006, **110**, 23701–23709.
66 V. R. Hathwar, S. M. Roopan, R. Subashini, F. N. Khan and T. N. Guru Row, *J. Chem. Sci.*, 2010, **122**, 677–685.
67 M. A. Spackman and D. Jayatilaka, *CrystEngComm*, 2009, **11**, 19–32.
68 M. A. Spackman and J. J. McKinnon, *CrystEngComm*, 2002, **4**, 378–392.
69 J. J. McKinnon, D. Jayatilaka and M. A. Spackman, *Chem. Commun.*, 2007, 3814–3816.
70 W. L. F. Armarego and C. L. L. Chai, *Purification of Laboratory Chemicals*, Butterworth-Heinemann, Oxford, 7th edn, 2017.
71 L. Krause, R. Herbst-Irmer, G. M. Sheldrick and D. Stalke, *J. Appl. Crystallogr.*, 2015, **48**, 3–10.
72 *CrysAlisPro Software System*, Rigaku Oxford Diffraction Ltd, Oxford, UK, 2022.
73 G. M. Sheldrick, *Acta Crystallogr., Sect. C: Struct. Chem.*, 2015, **71**, 3–8.
74 G. M. Sheldrick, *Acta Crystallogr., Sect. A: Found. Adv.*, 2015, **71**, 3–8.
75 C. F. Macrae, I. Sovago, S. J. Cottrell, P. T. A. Galek, P. McCabe, E. Pidcock, M. Platings, G. P. Shields, J. S. Stevens, M. Towler and P. A. Wood, *J. Appl. Crystallogr.*, 2020, **53**, 226–235.
76 P. R. Spackman, M. J. Turner, J. J. McKinnon, S. K. Wolff, D. J. Grimwood, D. Jayatilaka and M. A. Spackman, *J. Appl. Crystallogr.*, 2021, **54**, 1006–1011.
77 (*a*) CCDC 2515382: Experimental Crystal Structure Determination, 2026, DOI: 10.5517/ccdc.csd.cc2qfgc0; (*b*) CCDC 2515386: Experimental Crystal Structure Determination, 2026, DOI: 10.5517/ccdc.csd.cc2qfgh4; (*c*) CCDC 2515642: Experimental Crystal Structure Determination, 2026, DOI: 10.5517/ccdc.csd.cc2qfqrn; (*d*) CCDC 2515643: Experimental Crystal Structure Determination, 2026, DOI: 10.5517/ccdc.csd.cc2qfqsp; (*e*) CCDC 2529829: Experimental Crystal Structure Determination, 2026, DOI: 10.5517/ccdc.csd.cc2qxhdk.